AIAA 2002–2514

Two-dimensional Wave Analysis of the Discontinuous Galerkin Method with Non-Uniform Grids and Boundary Conditions

Fang Q. Hu
Department of Mathematics and Statistics
Old Dominion University, Norfolk, Virginia 23529

Harold L. Atkins
NASA Langley Research Center
Hampton, Virginia 23681

8th AIAA/CEAS Aeroacoustics Conference
June 17–19, 2002/Breckenridge, Colorado

AIAA 2002–2514

Two-dimensional Wave Analysis of the Discontinuous Galerkin Method with Non-Uniform Grids and Boundary Conditions

Fang Q. Hu*
Department of Mathematics and Statistics
Old Dominion University, Norfolk, Virginia 23529
Harold L. Atkins†
NASA Langley Research Center
Hampton, Virginia 23681

The eigenvalue problem for spatially propagating waves in a discontinuous Galerkin scheme is formulated for a system of two dimensional hyperbolic equations. Both the quadrilateral and triangular elements are considered. The numerical dispersion and numerical damping errors are calculated for various orders of the basis functions and directions of wave propagation. Spatial propagation properties of the physical as well as non-physical numerical modes are studied. In addition, numerical reflections at an interface of triangular and quadrilateral elements are found and reflection coefficients are estimated. Examples of direct numerical simulations that verify some of the theoretical properties found in this paper are presented.

Introduction

Recently, the discontinuous Galerkin formulation of the finite element method has been increasingly used in computational aeroacoustics (CAA) and computational electromagnetics (CEM) [1-4]. Compared to finite difference schemes, finite element methods have an advantage in handling complex geometries in practical and realistic problems. In most traditional finite element methods for hyperbolic systems, nodal based continuous basis functions are used [5-6]. As a result, inversion of a global mass matrix becomes necessary at each time step. Although the mass matrix is usually sparse, its inversion often makes the numerical implementation non-compact and creates difficulties when high order basis functions are used. The utilization of high order basis functions has been shown to be more efficient in reducing the numerical dispersion and numerical damping errors in finite element methods [6]. In the discontinuous Galerkin formulation, on the other hand, there is no need to invert a global matrix (see reference [1] for a recent review and the references cited therein). This makes the implementation of the discontinuous Galerkin method compact and more efficient for time dependent problems. In addition, high order basis functions can be used easily without any essential difficulty and even spectral accuracy becomes obtainable.

When partial differential equations in aeroacoustics problems are solved computationally, the numerical dispersion relation and the discrete eigenfunction are, inevitably, not exactly the same as their physical counter parts. It is important to analyze this discrepancy and to understand its consequences in computing the acoustic waves [4, 7-9]. In reference [4], a study on spatially propagating waves in a one-dimensional hyperbolic system has been presented. Some of previous works on the Fourier analysis by other researchers were also reviewed in [4]. It was shown, analytically, that the numerical dispersion relation in a discontinuous Galerkin method is locally accurate to the optimal order $2p+2$, where p is the highest order of the basis polynomials. Furthermore, for each physical mode, there is only one spurious non-physical mode. As a result, numerical reflections at a grid discontinuity, when they occur, are always in the form of the spurious non-physical mode and are highly damped.

In the present paper, the one dimensional study presented in [4] is extended to a system of two dimensional equations. The acoustic wave equation will be discretized using triangular, quadrilateral or a hybrid of these two types of elements. As we will see, the super-accuracy in the numerical dispersion relation is found to be true for two-

*Associate Professor, Senior Member AIAA
†Senior Research Scientist, Senior Member AIAA

dimensional waves as well. A methodology of comparing the discrete and exact eigenfunctions will be presented. The discrete eigenfunctions are found to be accurate to a global order of $p+1$ in a uniform grid. The results on the numerical eigensolutions are then applied to study numerical reflections at a grid discontinuity caused by a change in element topography. Here, a significant difference between the one- and two-dimensional waves occurs in that the numerically reflected waves in a two-dimensional problem can be in the form of the physical as well as the spurious non-physical modes. However, it will be shown that the amplitudes of reflected waves at the grid discontinuity decrease very rapidly as the mesh size decreases.

In the next section, the discontinuous Galerkin formulation for a linear two-dimensional hyperbolic system is briefly outlined. Then a Fourier analysis of the scheme in a uniform square or triangular grid is presented. The emphasis will be on the spatially propagating waves. By using the results of the uniform grids, numerical wave reflections at an interface of two different types of elements will be analyzed. Direct numerical simulation results that verify the theoretical findings will also be presented.

Discontinuous Galerkin formulation

Consider the discontinuous Galerkin method for a system of hyperbolic equations in two space dimensions $\mathbf{x} = (x, y)$:

$$\frac{\partial \mathbf{u}}{\partial t} + \nabla \cdot \mathbf{F}(\mathbf{u}) = 0 \tag{1}$$

where $\mathbf{u}$ is a vector of dimension N, $\mathbf{F} = (\mathbf{f}_1, \mathbf{f}_2)$ is the flux vector and $\nabla = (\frac{\partial}{\partial x}, \frac{\partial}{\partial y})$. Let the spatial domain be partitioned into elements Ω_K, i.e., $\Omega = \bigcup_K \Omega_K$. Within each element, the numerical solution, denoted by $\mathbf{u}_h$, is approximated by an expansion in the basis polynomials as

$$\mathbf{u}_h(\mathbf{x}, t) = \sum_{\ell=1}^{L} \mathbf{c}_\ell(t)\phi_\ell(\mathbf{x}), \tag{2}$$

where $\{\phi_\ell(\mathbf{x}), \ell = 1, 2, .., L\}$ is the set of the basis polynomials and $\mathbf{c}_\ell(t)$ is the expansion coefficient. For simplicity, the basis functions are chosen to be of the form $\{x^\alpha y^\beta | 0 \le \alpha + \beta \le p\}$, where p is the highest order of the polynomials. Thus,

$$L = \frac{1}{2}(p+1)(p+2).$$

We require that when (2) is substituted into (1), the residual is orthogonal to the basis functions, i.e.,

$$\int_{\Omega_K} \left(\frac{\partial \mathbf{u}_h}{\partial t} + \nabla \cdot \mathbf{F}(\mathbf{u}) \right) \phi_\ell(\mathbf{x}) d\mathbf{x} = 0$$

for $\ell = 1, 2, ..., L$. By a use of integration by parts, we get the following weak formulation,

$$\int_{\Omega_K} \phi_\ell(\mathbf{x}) \frac{\partial \mathbf{u}_h}{\partial t} d\mathbf{x} + \int_{\Gamma_K} \phi_\ell(\mathbf{x})(\mathbf{n} \cdot \mathbf{F}) ds$$

$$- \int_{\Omega_K} \nabla \phi_\ell(\mathbf{x}) \cdot \mathbf{F} d\mathbf{x} = 0 \tag{3}$$

where Γ_K denotes the edge of Ω_K and $\mathbf{n} = (n_1, n_2)$ is the outward normal. Equation (3) gives a system of ordinary differential equations for the expansion coefficients $\mathbf{c}_\ell(t)$. It is to be noted that the numerical solution is not required to be continuous across any interface between two elements. Instead, inter-element coupling is accomplished through the normal flux vector in the edge integral in (3). In this way, high order basis functions can be easily applied and the numerical implementation becomes compact [1-2].

We will only consider linear equations and assume that the flux vector is of the form

$$\mathbf{F}(\mathbf{u}) = (\mathbf{A}_1\mathbf{u}, \mathbf{A}_2\mathbf{u}) \tag{4}$$

where $\mathbf{A}_1$ and $\mathbf{A}_2$ are constant $N \times N$ matrices. To reflect the properties of the Euler equations, we further assume that $\mathbf{A}_1$ and $\mathbf{A}_2$ are not simultaneously diagonalizable. Moreover, we denote the normal flux Jacobian matrix by

$$\mathbf{A}_n = n_1\mathbf{A}_1 + n_2\mathbf{A}_2. \tag{5}$$

As noted earlier, since we do not require that the numerical solution be continuous across the interface of any two elements, the normal flux $\mathbf{n} \cdot \mathbf{F}$ appearing in the edge integral in (3) is not uniquely determined. To complete the formulation, a numerical flux formula needs to be specified. As in reference [4], we will consider two commonly used flux formulas, namely, the characteristics splitting flux formula and the Lax-Friedrichs flux formula. For convenience of discussion, let $\mathbf{u}_h^+$ and $\mathbf{u}_h^-$ denote the values of $\mathbf{u}_h$ on the edge of an element evaluated using numerical solutions inside and outside of that element respectively. For the characteristics splitting flux formula, the normal flux on the edge is computed as

$$\mathbf{n} \cdot \mathbf{F} = \frac{1}{2}\mathbf{A}_n(\mathbf{u}_h^+ + \mathbf{u}_h^-) - \frac{1}{2}|\mathbf{A}_n|(\mathbf{u}_h^- - \mathbf{u}_h^+) \tag{6}$$

where $\mathbf{A}_n$ is that given in (5). For the Lax-Friedrichs flux formula, the normal flux is computed as

$$\mathbf{n} \cdot \mathbf{F} = \frac{1}{2}\mathbf{A}_n(\mathbf{u}_h^+ + \mathbf{u}_h^-) - \frac{1}{2}|a_{max}|(\mathbf{u}_h^- - \mathbf{u}_h^+) \tag{7}$$

where a_{max} is the largest (in absolute value) eigenvalue of $\mathbf{A}_n$. It is easy to see that both flux formulas can be conveniently written in the form of

$$\mathbf{n} \cdot \mathbf{F} = \mathbf{A}_+ \mathbf{u}_h^+ + \mathbf{A}_- \mathbf{u}_h^- \tag{8}$$

where

$$\mathbf{A}_+ = \frac{1}{2}(\mathbf{A}_n + |\mathbf{A}_n|) \text{ and } \mathbf{A}_- = \frac{1}{2}(\mathbf{A}_n - |\mathbf{A}_n|)$$

for the characteristics splitting flux formula and

$$\mathbf{A}_+ = \frac{1}{2}(\mathbf{A}_n + |a_{max}|\mathbf{I}_N) \text{ and } \mathbf{A}_- = \frac{1}{2}(\mathbf{A}_n - |a_{max}|\mathbf{I}_N)$$

for the Lax-Friedrichs flux formula. Here $\mathbf{I}_N$ denotes the $N \times N$ identity matrix

Quadrilateral elements

Consider a discretization with uniformly distributed quadrilateral elements. For simplicity, the elements will be taken to be squares with each side of length h. The analysis lends itself easily to more general quadrilateral elements. In addition, we introduce element indices n and m in the x and y directions respectively and denote each element by Ω_{nm} and its four boundaries $\Gamma_{nm}^{(i)}$, $i = 1, 2, 3, 4$, as shown in Figure 1. Using (8) for the normal flux, the weak formulation (3) can be written as

$$\begin{aligned} &\int_{\Omega_{nm}} \phi_\ell(\mathbf{x}) \frac{\partial \mathbf{u}_h^{nm}}{\partial t} d\mathbf{x} + \int_{\Gamma_{nm}^{(1)}} \phi_\ell(\mathbf{x})(\mathbf{A}_+^{(1)} \mathbf{u}_h^{nm} + \mathbf{A}_-^{(1)} \mathbf{u}_h^{nm-1}) ds \\ &+ \int_{\Gamma_{nm}^{(2)}} \phi_\ell(\mathbf{x})(\mathbf{A}_+^{(2)} \mathbf{u}_h^{nm} + \mathbf{A}_-^{(2)} \mathbf{u}_h^{n+1m}) ds \\ &+ \int_{\Gamma_{nm}^{(3)}} \phi_\ell(\mathbf{x})(\mathbf{A}_+^{(3)} \mathbf{u}_h^{nm} + \mathbf{A}_-^{(3)} \mathbf{u}_h^{nm+1}) ds \\ &+ \int_{\Gamma_{nm}^{(4)}} \phi_\ell(\mathbf{x})(\mathbf{A}_+^{(4)} \mathbf{u}_h^{nm} + \mathbf{A}_-^{(4)} \mathbf{u}_h^{n-1m}) ds \\ &- \int_{\Omega_{nm}} \frac{d\phi_\ell}{dx} \mathbf{A}_1 \mathbf{u}_h^{nm} d\mathbf{x} - \int_{\Omega_{nm}} \frac{d\phi_\ell}{dy} \mathbf{A}_2 \mathbf{u}_h^{nm} d\mathbf{x} = 0 \end{aligned} \tag{9}$$

for $\ell = 1, 2, ..., L$, where superscripts $(1) - (4)$ indicate the specific edge of the element.

To look for wave-like solutions supported by (9), we assume periodicity in time with a frequency ω and let

$$\mathbf{u}_h^{nm}(x, y, t) = e^{-i\omega t} \hat{\mathbf{u}}_h^{nm}(x, y), \tag{10}$$

where

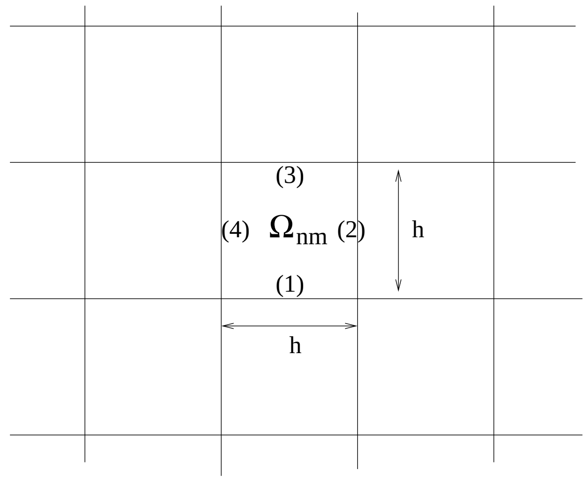

Figure 1 A schematic of partitioning of the computational domain in quadrilateral elements. Here, n and m are the indices of the element and the number inside the parentheses indicates the ordering of the element edges.

$$\hat{\mathbf{u}}_h^{nm}(x, y) = \sum_{\ell=1}^{L} \hat{\mathbf{c}}_\ell^{nm} \phi_\ell(x, y). \tag{11}$$

The coefficients $\hat{\mathbf{c}}_\ell^{nm}$ are now independent of t.

For convenience of discussion, define vectors

$$\hat{\mathbf{C}}^{nm} = \begin{pmatrix} \hat{\mathbf{c}}_1^{nm} \\ \hat{\mathbf{c}}_2^{nm} \\ \vdots \\ \hat{\mathbf{c}}_L^{nm} \end{pmatrix}_{NL \times 1}$$

and

$$\mathbf{P} = \begin{pmatrix} \phi_1 \\ \phi_2 \\ \vdots \\ \phi_L \end{pmatrix}_{L \times 1}.$$

Then, using the Kronecker product $\otimes$(see reference [4] for definition), the solution in (11) can be expressed as follows,

$$\hat{\mathbf{u}}_h^{nm} = (\mathbf{P}^T \otimes \mathbf{I}_N) \hat{\mathbf{C}}^{nm}. \tag{12}$$

By substituting (10) into (9), we get a linear system for the expansion coefficients $\hat{\mathbf{C}}^{nm}$ as follows:

$$\begin{aligned} &-i\omega(\mathbf{Q} \otimes \mathbf{I}_N)\hat{\mathbf{C}}^{nm} + (\mathbf{B}^{(1)} \otimes \mathbf{A}_+^{(1)})\hat{\mathbf{C}}^{nm} + (\mathbf{B}'^{(1)} \otimes \mathbf{A}_-^{(1)})\hat{\mathbf{C}}^{nm-1} \\ &+ (\mathbf{B}^{(2)} \otimes \mathbf{A}_+^{(2)})\hat{\mathbf{C}}^{nm} + (\mathbf{B}'^{(2)} \otimes \mathbf{A}_-^{(2)})\hat{\mathbf{C}}^{n+1m} \\ &+ (\mathbf{B}^{(3)} \otimes \mathbf{A}_+^{(3)})\hat{\mathbf{C}}^{nm} + (\mathbf{B}'^{(3)} \otimes \mathbf{A}_-^{(3)})\hat{\mathbf{C}}^{nm+1} \end{aligned}$$

$$+(\mathbf{B}^{(4)} \otimes \mathbf{A}_+^{(4)})\hat{\mathbf{C}}^{nm} + (\mathbf{B}'^{(4)} \otimes \mathbf{A}_-^{(4)})\hat{\mathbf{C}}^{n-1m}$$

$$-(\mathbf{Q}_x \otimes \mathbf{A}_1)\hat{\mathbf{C}}^{nm} - (\mathbf{Q}_y \otimes \mathbf{A}_2)\hat{\mathbf{C}}^{nm} = 0 \qquad (13)$$

where $\mathbf{Q}$ is the mass matrix, $\mathbf{Q}_x$ and $\mathbf{Q}_y$ are the "stiffness" matrices, and $\mathbf{B}^{(i)}$ and $\mathbf{B}'^{(i)}$ are obtained from the edge integrals for solutions inside and outside of the element respectively. The detailed definitions of these matrices are given in the Appendix.

Equation (13) can be written more intuitively as

$$-i\omega\bar{\mathbf{Q}}\hat{\mathbf{C}}^{nm} + \mathbf{H}^{(0)}\hat{\mathbf{C}}^{nm} + \mathbf{H}^{(1)}\hat{\mathbf{C}}^{nm-1} + \mathbf{H}^{(2)}\hat{\mathbf{C}}^{n+1m}$$

$$+\mathbf{H}^{(3)}\hat{\mathbf{C}}^{nm+1} + \mathbf{H}^{(4)}\hat{\mathbf{C}}^{n-1m} = 0 \qquad (14)$$

where

$$\bar{\mathbf{Q}} = \mathbf{Q}\otimes\mathbf{I}_N,\ \ \mathbf{H}^{(0)} = \sum_{i=1}^{4}\mathbf{B}^{(i)}\otimes\mathbf{A}_+^{(i)} - \mathbf{Q}_x\otimes\mathbf{A}_1 - \mathbf{Q}_y\otimes\mathbf{A}_2,$$

$$\text{and } \mathbf{H}^{(i)} = \mathbf{B}'^{(i)} \otimes \mathbf{A}_-^{(i)},\ i = 1,2,3,4.$$

Since we have a uniform distribution of elements, the coefficient matrices in (14) are independent of the element indices n and m. We seek solutions of the form

$$\hat{\mathbf{C}}^{nm} = \lambda_1^n \lambda_2^m \tilde{\mathbf{C}} \qquad (15)$$

where $\tilde{\mathbf{C}}$ is independent of the element indices n and m. Substituting (15) into (14), we get a homogeneous system for $\tilde{\mathbf{C}}$:

$$-i\omega\bar{\mathbf{Q}}\tilde{\mathbf{C}} + \mathbf{H}^{(0)}\tilde{\mathbf{C}} + \frac{1}{\lambda_2}\mathbf{H}^{(1)}\tilde{\mathbf{C}} + \lambda_1\mathbf{H}^{(2)}\tilde{\mathbf{C}}$$

$$+\lambda_2\mathbf{H}^{(3)}\tilde{\mathbf{C}} + \frac{1}{\lambda_1}\mathbf{H}^{(4)}\tilde{\mathbf{C}} = 0. \qquad (16)$$

We note that the values of λ_1 and λ_2 are related to wavenumbers k_1 and k_2, respectively, by expressions

$$\lambda_1 = e^{ik_1 h}, \quad \lambda_2 = e^{ik_2 h}. \qquad (17)$$

To study the spatially propagating waves, we solve for λ_1 and $\tilde{\mathbf{C}}$ as the eigenvalue and eigenvector for given ω and λ_2. Specifically, when k_2 is chosen to be of the form $k_2 = \omega\sin\theta$, the resulting eigensolution will approximate a plane wave of angle θ. The corresponding discrete eigenfunction is constructed according to (10) and (11). The details are omitted here.

Triangular elements

We now consider the eigenvalue problem when the spatial domain is partitioned by triangular elements. We assume that the triangulation is spatially periodic with triangles of types (a) and (b) being repeated in the x and y directions, as shown in Figure 2. The elements will be denoted by $\Omega_{nm}^{(a)}$ or $\Omega_{nm}^{(b)}$ accordingly. The numerical solutions are expanded as

$$\mathbf{u}_h^{(a)nm}(\mathbf{x},t) = \sum_{\ell=1}^{L}\mathbf{c}_\ell^{(a)nm}(t)\psi_\ell(\mathbf{x})$$

in $\Omega_{nm}^{(a)}$ and

$$\mathbf{u}_h^{(b)nm}(\mathbf{x},t) = \sum_{\ell=1}^{L}\mathbf{c}_\ell^{(b)nm}(t)\psi_\ell(\mathbf{x})$$

in $\Omega_{nm}^{(b)}$, where $\psi_\ell(\mathbf{x})$ are the basis functions for triangular elements.

Then, by (3), the discontinuous Galerkin weak formulation for elements of type (a) becomes

$$\int_{\Omega_{nm}^{(a)}}\psi_\ell(\mathbf{x})\frac{\partial\mathbf{u}_h^{(a)nm}}{\partial t}d\mathbf{x}$$

$$+\int_{\Gamma_{nm}^{(a)(1)}}\psi_\ell(\mathbf{x})(\mathbf{A}_+^{(1)}\mathbf{u}_h^{(a)nm} + \mathbf{A}_-^{(1)}\mathbf{u}_h^{(b)nm-1})ds$$

$$+\int_{\Gamma_{nm}^{(a)(2)}}\psi_\ell(\mathbf{x})(\mathbf{A}_+^{(2)}\mathbf{u}_h^{(a)nm} + \mathbf{A}_-^{(2)}\mathbf{u}_h^{(b)nm})ds$$

$$+\int_{\Gamma_{nm}^{(a)(3)}}\psi_\ell(\mathbf{x})(\mathbf{A}_+^{(3)}\mathbf{u}_h^{(a)nm} + \mathbf{A}_-^{(3)}\mathbf{u}_h^{(b)n-1m})ds$$

$$-\int_{\Omega_{nm}^{(a)}}\frac{d\psi_\ell}{dx}\mathbf{A}_1\mathbf{u}_h^{(a)nm}d\mathbf{x} - \int_{\Omega_{nm}^{(a)}}\frac{d\psi_\ell}{dy}\mathbf{A}_2\mathbf{u}_h^{(a)nm}d\mathbf{x} = 0 \qquad (18)$$

for $\ell = 1,2,...,L$. Similar equations for elements of type (b) can be obtained easily.

By assuming a time periodicity similar to (10) and introducing vectors

$$\hat{\mathbf{C}}_a^{nm} = \begin{pmatrix}\hat{\mathbf{c}}_1^{(a)nm}\\ \hat{\mathbf{c}}_2^{(a)nm}\\ \vdots\\ \hat{\mathbf{c}}_L^{(a)nm}\end{pmatrix},\ \ \hat{\mathbf{C}}_b^{nm} = \begin{pmatrix}\hat{\mathbf{c}}_1^{(b)nm}\\ \hat{\mathbf{c}}_2^{(b)nm}\\ \vdots\\ \hat{\mathbf{c}}_L^{(b)nm}\end{pmatrix},$$

a linear system that couples $\hat{\mathbf{C}}_a^{nm}$ and $\hat{\mathbf{C}}_b^{nm}$ can be formed as follows,

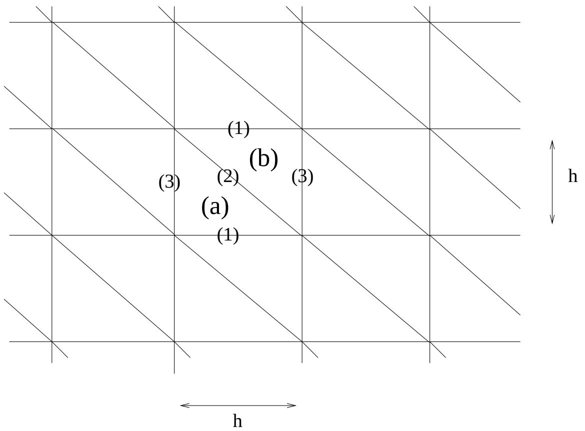

Figure 2 Schematic of uniform distribution of triangular elements. Numbers inside the parenthesis indicates the ordering of the sides.

$$-i\omega\bar{\mathbf{Q}}_a\hat{\mathbf{C}}_a^{nm} + \mathbf{H}_a^{(0)}\hat{\mathbf{C}}_a^{nm} + \mathbf{H}_a^{(1)}\hat{\mathbf{C}}_b^{nm-1} + \mathbf{H}_a^{(2)}\hat{\mathbf{C}}_b^{nm} + \mathbf{H}_a^{(3)}\hat{\mathbf{C}}_b^{n-1m} = 0 \tag{19}$$

and

$$-i\omega\bar{\mathbf{Q}}_b\hat{\mathbf{C}}_b^{nm} + \mathbf{H}_b^{(0)}\hat{\mathbf{C}}_b^{nm} + \mathbf{H}_b^{(1)}\hat{\mathbf{C}}_a^{nm+1} + \mathbf{H}_b^{(2)}\hat{\mathbf{C}}_a^{nm} + \mathbf{H}_b^{(3)}\hat{\mathbf{C}}_a^{n+1m} = 0. \tag{20}$$

An eigenvalue problem similar to (16) can be formed in a straight forward manner.

Waves in uniform grids

To demonstrate wave propagation properties of the discontinuous Galerkin method in two space dimensions, we will use the following system of equations for all the numerical results presented in this paper:

$$\frac{\partial \mathbf{u}}{\partial t} + \mathbf{A}_1\frac{\partial \mathbf{u}}{\partial x} + \mathbf{A}_2\frac{\partial \mathbf{u}}{\partial y} = 0 \tag{21}$$

where

$$\mathbf{A}_1 = \begin{pmatrix} 1 & 0 \\ 0 & 1 \end{pmatrix}, \qquad \mathbf{A}_2 = \begin{pmatrix} 0 & 1 \\ -1 & 0 \end{pmatrix}. \tag{22}$$

It can be shown easily that this system is equivalent to the more familiar second order two-dimensional wave equation

$$\frac{\partial^2 u}{\partial t^2} + \frac{\partial^2 u}{\partial x^2} + \frac{\partial^2 u}{\partial y^2} = 0.$$

For a plane wave of the form

$$\mathbf{u} = \hat{\mathbf{u}}e^{ik_1x+ik_2y-i\omega t},$$

the exact dispersion relation for (21) is

$$\omega^2 = k_1^2 + k_2^2 \tag{23}$$

where k_1 and k_2 are wavenumbers in the x and y directions respectively. The exact eigensolution of (21)-(22) can be expressed as

$$\mathbf{f} = \begin{pmatrix} 1+\cos\theta \\ \sin\theta \end{pmatrix} e^{i\omega\cos\theta x + i\omega\sin\theta y - i\omega t} \tag{24}$$

where θ is the angle of wave propagation.

Dispersion and dissipation errors

When equation (21) is solved numerically, the numerical dispersion relation and the discrete eigenfunction are, inevitably, not exactly the same as (23). Most notably there will be spurious numerical modes in addition to the physical modes. The numerical dispersion relation can be found from the homogeneous system formulated in previous sections, i.e., equation (16) for square elements or equations (19) and (20) for triangular elements. A generalized algebraic eigenvalue problem can be formed for one of the three parameters in the system, namely, ω, λ_1 and λ_2. Note in particular that λ_1 and λ_2 are related to the spatial wavenumbers k_1 and k_2 by equation (17). For an initial value problem, the values of k_1 and k_2 are given and ω is found as the eigenvalue [7-9]. However, to study wave propagation in non-uniform grids, it becomes necessary to consider spatially propagating waves since the wavenumber will not remain constant. Therefore, we will treat the homogeneous system as an eigenvalue problem for λ_1 for given values of ω and $\lambda_2 = e^{ik_2h}$. Once λ_1 is found, the numerical wavenumber, denoted by k_1^*, is obtained as

$$k_1^*h = -i\ln(\lambda_1).$$

In general, k_1^* is complex, i.e., $k_1^* = k_{1r}^* + ik_{1i}^*$. The imaginary part of k_1^* represents the dissipation of the wave as it propagates in space. The real part of k_1^* should be close to the exact physical wavenumber, namely, $k_{1r}^{*2} \approx \omega^2 - k_2^2$.

In addition to the physically meaningful eigenvalues, there are also spurious non-physical wave modes. It can be shown that the linear homogeneous systems obtained in the previous sections will have $N(p+1)$ eigenvalues where N is the number of equations in the physical system (1) and p is the order of the basis polynomials. The situation for $p=2$ is illustrated in Figure 3 and Figure 4. The real and imaginary parts of numerical wave number k_1^* are plotted as functions of the frequency ω. For this calculation,

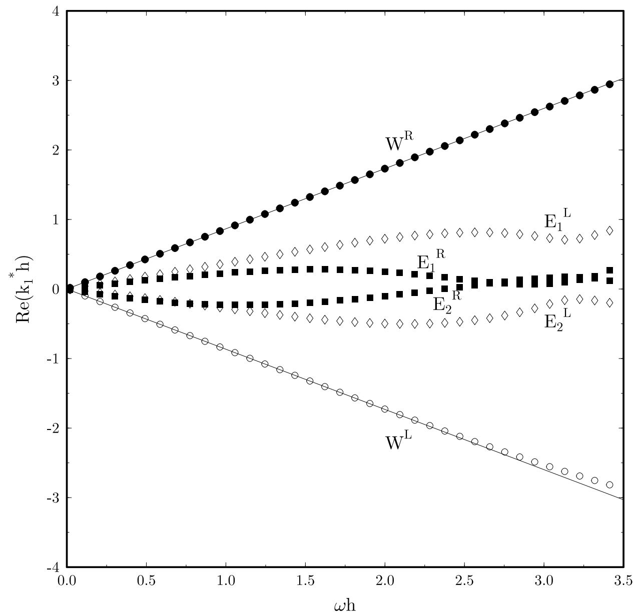

Figure 3 Real part of numerical wave numbers. Triangular elements. $p = 2$, $k_2 = \omega \sin(\theta)$, $\theta = \pi/6$. —— exact dispersion relation, • physical right-traveling mode (W^R), ∘ physical left-traveling mode (W^L), ▪ right-traveling non-physical modes (E_1^R, E_2^R), ⋄ left-traveling non-physical modes (E_1^L, E_2^L).

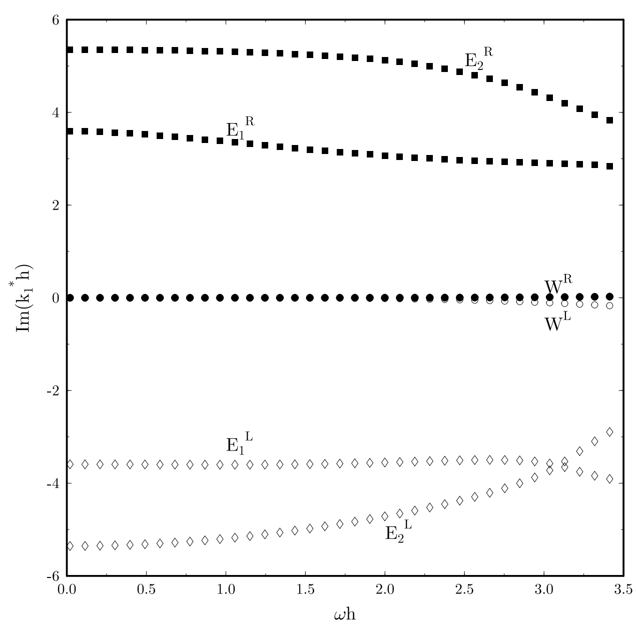

Figure 4 Imaginary part of numerical wave numbers. See Figure 3 for caption.

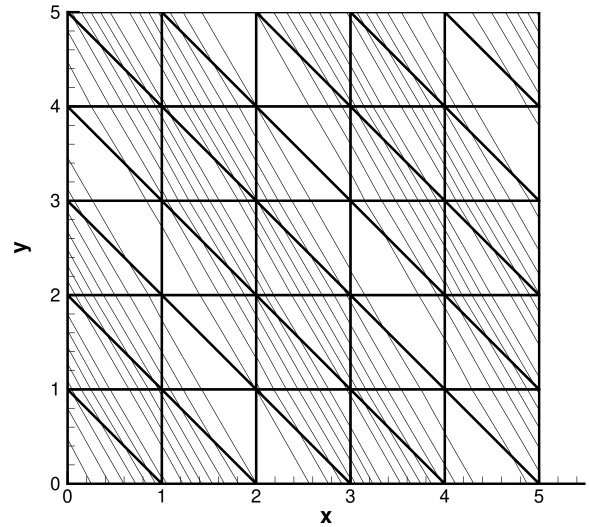

Figure 5 Contours of the discrete eigenfunction in a uniform triangular mesh. Physical mode W^R for $\omega h = \pi/2$, $k_2 = \omega \sin(\pi/6)$, $p = 2$.

$k_2 = \omega \sin(\pi/6)$. There are six eigenmodes. Two of the modes, labeled W^R and W^L, closely resemble the physical right-traveling and left-traveling waves, respectively. The other four modes, two right-traveling (E_1^R, E_2^R) and two left-traveling (E_1^L, E_2^L), are spurious non-physical waves. However, it is important to note that, as Figure 4 shows, the non-physical waves have large damping rates, which render them inefficient in propagation.

The contours of the discrete eigenfunction for the physical wave mode W^R are shown in Figure 5. To further study the physical modes, let's define numerical phase speed as

$$c_{ph} = \frac{\omega}{\sqrt{k_{1r}^{*2} + k_2^2}}.$$

Clearly, c_{ph} will depend on ω and k_2, giving rise to dispersion errors in the numerical solution. Figure 6 shows c_{ph} as a function of non-dimensionalized frequency ωh^*, where a value of $k_2 = \omega \sin(\pi/6)$ has been assumed. The results for triangular elements are shown in solid lines while those for quadrilateral elements are shown in dashed lines. For a fair comparison of the two types of elements, the frequency has been non-dimensionalized by h^*:

$$h^* = \begin{cases} h & \text{triangular} \\ \frac{1}{\sqrt{2}}h & \text{quadrilateral} \end{cases}.$$

This is to ensure that, for any given computational domain, the two types of elements would use the same number of unknowns when the order of basis functions is kept

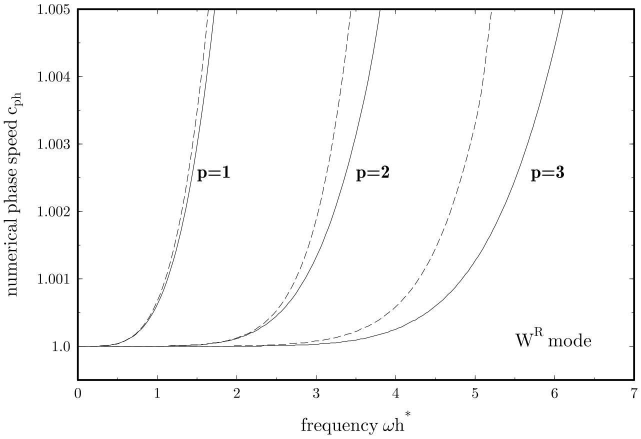

Figure 6 Numerical phase speed of the physical mode W^R. $\theta = \pi/6$. Solid lines for triangular elements and dashed lines for quadrilateral elements. p is the order of basis polynomials.

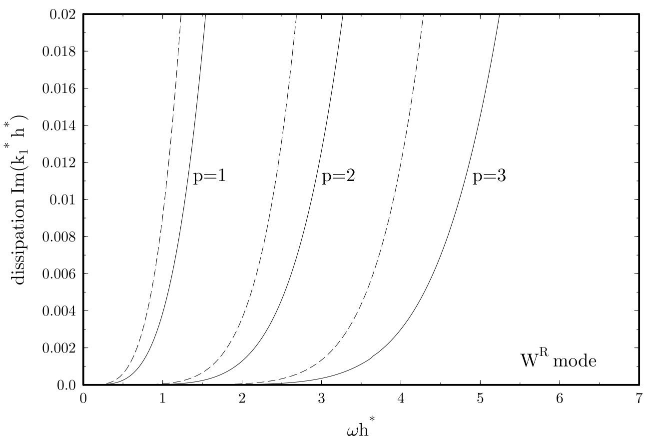

Figure 7 Dissipation errors of the physical mode W^R. $\theta = \pi/6$. Solid lines for triangular elements and dashed lines for quadrilateral elements. p is the order of basis polynomials.

the same. In all the cases, increasing the order of the basis functions results in significant improvement in phase speed and dissipation errors. For the chosen angle of wave propagation $\theta = \pi/6$, Figure 6 shows that triangular elements have a some what better performance in the phase speed. The comparisons in dissipation error are shown in Figure 7. Again, triangular elements result in smaller dissipation error.

However, we should note that the damping factor for triangular elements, with a pattern as shown in Figure 2, exhibits stronger preference in the direction of wave propagation [7]. In Figures 8 and 9, we show the directivity plot of the damping factor for $0 \leq \theta \leq \pi$ after a propagation of 10 wavelengths. Therefore, for waves whose propagation direction θ is in the second quadrant, for in-

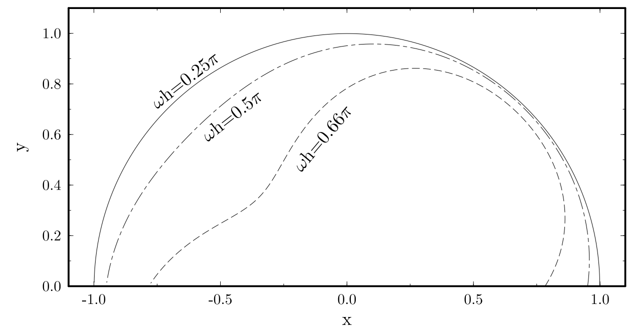

Figure 8 Directivity plot of damping factor $e^{-10\lambda k_{1i}}$ for $\lambda = 8h, 4h$ and $3h$ where λ is the wavelength and h is the element size defined in Figure 2. Triangular elements. $p = 2$.

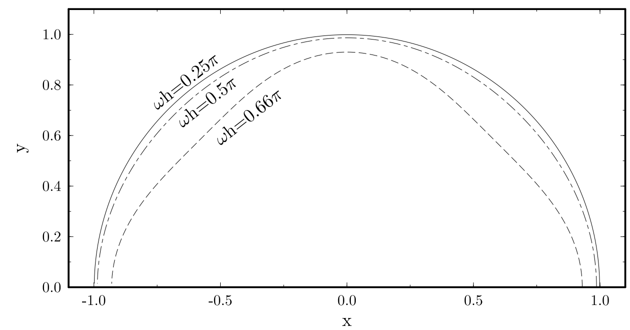

Figure 9 Directivity plot of damping factor $e^{-10\lambda k_{1i}}$ for square elements. $p = 2$. Wavelength λ is the same as those in Figure 8.

stance $\theta = 5\pi/6$, the advantage of triangles over squares shown in Figures 6 and 7 for $\theta = \pi/6$ is expected to be reversed.

It is interesting to compare the phase error of the discontinuous Galerkin method with that of finite difference schemes. In Figure 10, the numerical phase speed c_{ph} as a function of non-dimensionalized frequency is plotted for the 4th order central and compact finite difference schemes, as well as the 4th-order (p=3) discontinuous Galerkin scheme with triangular elements. Here, when angle $\theta = 0$, the finite difference schemes are assumed to have a grid spacing of $\Delta x = h/4$ where h is the dimension of triangular elements. We see that, while DGM schemes produce waves that travel faster than the exact phase speed, the finite difference schemes have a phase lag in the solution. However, the phase error is much smaller in the DGM scheme.

In reference [4], it has been shown, for a one dimensional system, that the real part of the numerical wave number is accurate *locally* to order $2p + 3$ and the imaginary part accurate *locally* to order $2p + 2$. This is again observed in

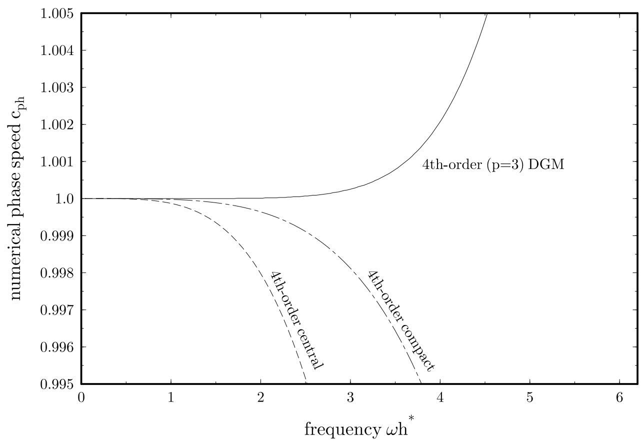

Figure 10 Comparison of numerical phase speed for 4-th order finite difference and discontinuous Galerkin schemes.

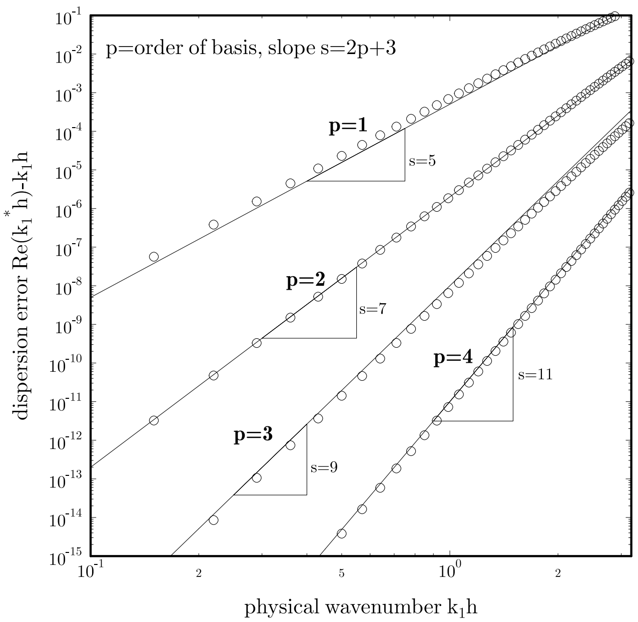

Figure 11 Convergence of the real part of k_1^*. p is the order of basis functions and s is the slope of the fitted line. Triangular elements.

two dimensional waves in this paper. In Figures 11 and 12 we show the convergence of the real and imaginary parts of the numerical wavenumber k_1^*. The slope of convergence in the log-log scale is indicated in the figures by s.

Convergence of eigenfunctions

We now consider the convergence of the discrete eigenfunctions. For a wave equation written in the form of (21), the exact eigenfunction is given in (24).

To obtain the order property on the convergence of the discrete eigenfunction, we form a correlation coefficient α

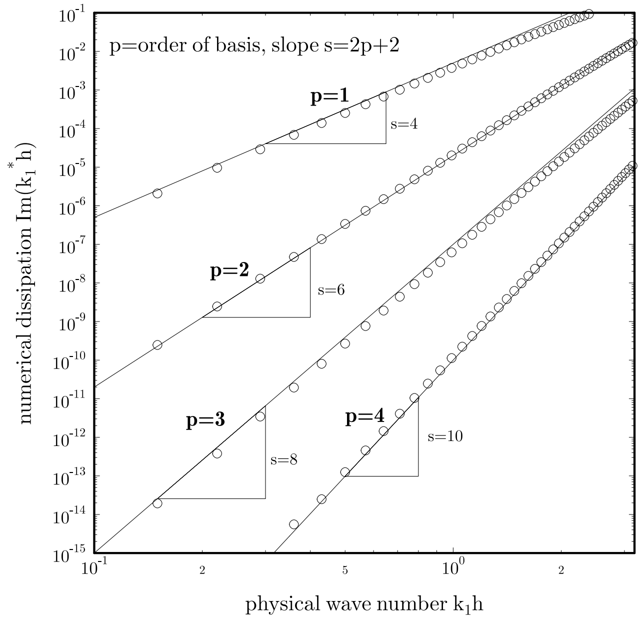

Figure 12 Convergence of imaginary part of k_1^*. p is the order of basis functions and s is the slope of the fitted line. Triangular elements.

as follows,

$$\alpha = \frac{< \mathbf{f}, \mathbf{u}_h >}{\sqrt{< \mathbf{f}, \mathbf{f} >< \mathbf{u}_h, \mathbf{u}_h >}}$$

where the inner product is defined as

$$< \mathbf{u}, \mathbf{v} >= \int_\Omega \mathbf{u} \cdot \mathbf{v}^* d\mathbf{x}.$$

Coefficient α is meaningful because it can be shown that $|\alpha| = 1$ if and only if $\mathbf{u}_h$ is proportional to $\mathbf{f}$. Furthermore, the L_2 norm of the projection error from the exact eigenfunction to the discrete eigenfunction is found to be related to α as

$$E_2 = \sqrt{< \mathbf{f} - c\mathbf{u}_h, \mathbf{f} - c\mathbf{u}_h >} = \sqrt{(1-|\alpha|)(1+|\alpha|)|\mathbf{f}|^2} \tag{25}$$

where $c =< \mathbf{f}, \mathbf{u}_h > / < \mathbf{u}_h, \mathbf{u}_h >$. The L_2 norm E_2 is found to decay at order $p+1$ as shown in Figure 13. This order property has been verified for a flux formula that is of either characteristics-based or Lax-Friedrichs type.

Coupling of triangular and quadrilateral elements

In practical computations, the grids are likely to be non-uniform and may even be a hybrid of triangles and squares.

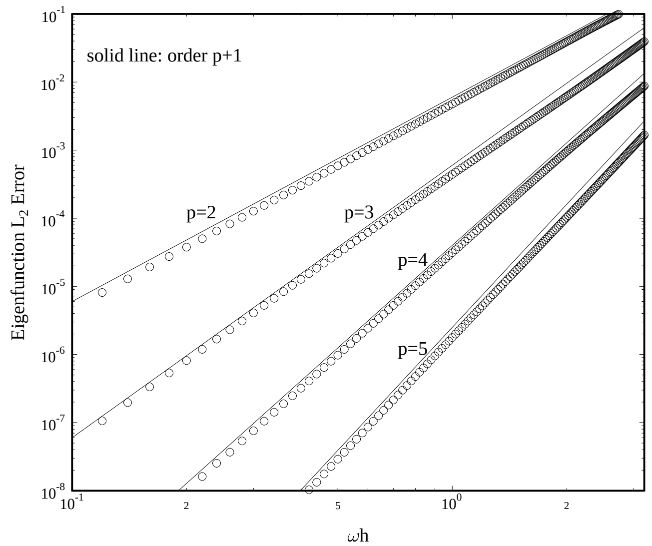

Figure 13 Convergence of eigenfunctions. p is the highest order of the basis polynomials. For this calculation, the discrete eigenfunction is found by choosing $k_2 = \omega \sin(\pi/3)$. ωh is the non-dimensionalized frequency where h is the element size. $\circ$ error in L_2 norm computed by (25), —— order $p+1$ convergence line.

In this section, the eigensolutions analyzed in the preceding sections will be used to study a particular scenario of non-uniform grids. We will consider the coupling of numerical solutions at an interface of triangular and quadrilateral elements, as shown in Figure 14. Due to discontinuity in grid topography, spurious numerical reflections can occur at the interface.

Let the elements in the triangular and square half-domains be denoted by $\Omega_{nm}^{(a)}$, $\Omega_{nm}^{(b)}$ or Ω_{nm} , respectively, where n and m are element indices. Without loss of generality, suppose that the triangular elements are used for $n \leq 0$ and quadrilateral elements are used for $n \geq 1$. To introduce a right-going incident wave for $n \leq 0$, let the eigenfunctions for a right-traveling wave, mode W^R in Figure 3, be denoted as $\mathbf{V}_{a,W^R}^{nm}$ and $\mathbf{V}_{b,W^R}^{nm}$ for elements $\Omega_{nm}^{(a)}$ and $\Omega_{nm}^{(b)}$ respectively. Then, by including the reflected and transmitted waves, the solutions at the left and right of the interface can be expressed as

$n \leq 0$:

$$\hat{\mathbf{C}}_a^{nm} = \mathbf{V}_{a,W^R}^{nm} + \beta_{W^L}\mathbf{V}_{a,W^L}^{nm} + \sum_j \beta_{E_j^L}\mathbf{V}_{a,E_j^L}^{nm}, \qquad (26)$$

$$\hat{\mathbf{C}}_b^{nm} = \mathbf{V}_{b,W^R}^{nm} + \beta_{W^L}\mathbf{V}_{b,W^L}^{nm} + \sum_j \beta_{E_j^L}\mathbf{V}_{b,E_j^L}^{nm}, \qquad (27)$$

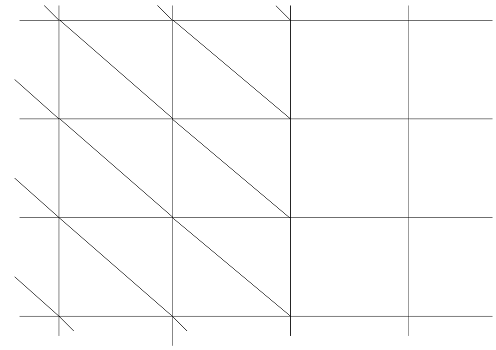

Figure 14 Schematic of an interface between triangular and square elements.

$n \geq 1$:

$$\hat{\mathbf{C}}^{nm} = \beta_{W^R}\mathbf{V}_{W^R}^{nm} + \sum_j \beta_{E_j^R}\mathbf{V}_{E_j^R}^{nm}, \qquad (28)$$

where β_{W^L} and $\beta_{E_j^L}$ are the reflection coefficients of the physical and spurious waves in the triangular elements respectively, and β_{W^R} and $\beta_{E_j^R}$ are the transmission coefficients of the right-traveling physical and spurious waves in the square elements respectively. The $\mathbf{V}$ vectors in (26)-(28) denote the corresponding eigenvectors. At elements next to the interface, the discretized equations (14) and (20) are modified due to the coupling between triangular elements of type (b) and quadrilateral elements. Specifically, we get

at $n = 0$:

$$-i\omega\bar{\mathbf{Q}}_b\hat{\mathbf{C}}_b^{0m} + \mathbf{H}_b^{(0)}\hat{\mathbf{C}}_b^{0m} + \mathbf{H}_b^{(1)}\hat{\mathbf{C}}_a^{0m+1} + \mathbf{H}_b^{(2)}\hat{\mathbf{C}}_a^{0m} + \tilde{\mathbf{H}}_b^{(3)}\hat{\mathbf{C}}^{1m} = 0 \qquad (29)$$

at $n = 1$:

$$-i\omega\bar{\mathbf{Q}}\hat{\mathbf{C}}^{1m} + \mathbf{H}^{(0)}\hat{\mathbf{C}}^{1m} + \mathbf{H}^{(1)}\hat{\mathbf{C}}^{1m-1} + \mathbf{H}^{(2)}\hat{\mathbf{C}}^{2m} + \mathbf{H}^{(3)}\hat{\mathbf{C}}^{1m+1} + \tilde{\mathbf{H}}^{(4)}\hat{\mathbf{C}}_b^{0m} = 0 \qquad (30)$$

where a tilde indicates modified matrices. In particular, we have

$$\tilde{\mathbf{H}}_b^{(3)} = \tilde{\mathbf{B}}_b'^{(3)} \otimes \mathbf{A}_-^{(3)}$$

and

$$\tilde{\mathbf{H}}^{(4)} = \tilde{\mathbf{B}}'^{(4)} \otimes \mathbf{A}_-^{(4)}$$

where the modified boundary integral matrices $\tilde{\mathbf{B}}_b'^{(3)}$ and $\tilde{\mathbf{B}}'^{(4)}$ are as follows,

$$\tilde{\mathbf{B}}_b'^{(3)} = \left\{ \int_{\Gamma_b^{(3)}} \psi_\ell \phi_{\ell'}^- ds \right\}$$

and

$$\tilde{\mathbf{B}}'^{(4)} = \left\{ \int_{\Gamma^{(4)}} \phi_\ell \psi_{\ell'}^- ds \right\}.$$

Here ψ_ℓ and ϕ_ℓ are basis functions used for triangular and quadrilateral elements respectively. After comparing with equations (20) and (14), equations (29) and (30) can be further simplified to be

$$\tilde{\mathbf{H}}_b^{(3)} \hat{\mathbf{C}}^{1m} = \mathbf{H}_b^{(3)} \hat{\mathbf{C}}_b^{1m}, \tag{31}$$

$$\tilde{\mathbf{H}}^{(4)} \hat{\mathbf{C}}_b^{0m} = \mathbf{H}^{(4)} \hat{\mathbf{C}}^{0m}. \tag{32}$$

This gives the matching conditions at the interface. By substituting (26)-(28) into the matching conditions, the reflection and transmission coefficients can be found.

The case of $p = 2$ is shown in Figure 15 where the reflection coefficients of the physical and spurious modes are plotted as functions of the non-dimensional incident wave frequency ωh. As ωh decreases, the resolution of the schemes on both sides of the interface is increased. As a result, as Figure 15 shows, the numerical reflection reduces significantly. More importantly, while the maximum reflection coefficient has been found to decay at order $p+1$, the amplitude of the reflected physical mode, W^L, is reduced much faster than that of the spurious modes (close to order $2p+1$). This has been found to be true for other values of p as well. This observation is significant because, as we have seen in Figure 4, the spurious waves are highly damped and inefficient in propagation. It indicates that numerical reflection occurring at the interface is likely to have only a local effect.

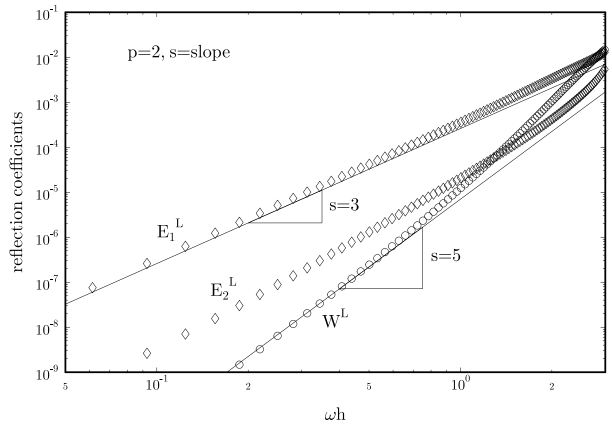

Figure 15 Magnitudes of reflection coefficients of the physical (W^L) and spurious (E_1^L, E_2^L) left traveling waves.

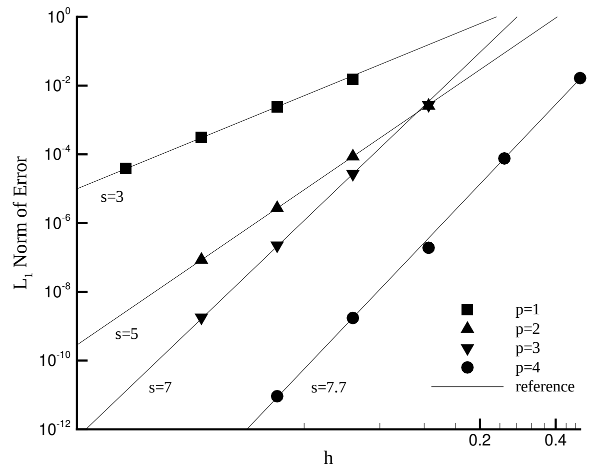

Figure 16 Mesh refinement results using uniform triangular elements shown in Figure 2. p is the order of the basis functions and s denotes the slope of the fitted convergence line.

Numerical Examples

In this section, we present results of direct numerical simulations of wave propagation in a discontinuous Galerkin scheme. In all the examples, equation (21) is solved by a quadrature-free implementation, which is detailed in reference [2]. The simulation has been carried out using two different mesh configurations. The first mesh configuration is a uniform mesh of triangles as shown in Figure 2. The second configuration uses a mix of triangles and squares as shown in Figure 14.

For numerical examples using uniform triangular elements, a computational domain of $[0,1] \times [0,1]$ is discretized with $h = 1/N$ where $2N^2$ is the total number of triangular elements. The computational domain is initialized with a plane wave given in equation (24). The wavelength is chosen such that periodic boundary conditions can be applied in both the x and y directions.

The initial values of the expansion coefficients in each element are obtained by projection. As the numerical solution advances in time, the values of $\mathbf{u}$ at 50×50 selected locations are sampled at time $t_n = nT$ where T is the period of the wave and $n = 1, 2, 3, ...20$. Then, solutions at t_n are compared with that at the final time t_{20} by computing the L_1 norm of their differences. In this way, the propagation errors, rather than the projection errors, can be assessed.

In Figure 16, we show the mesh refinement results for

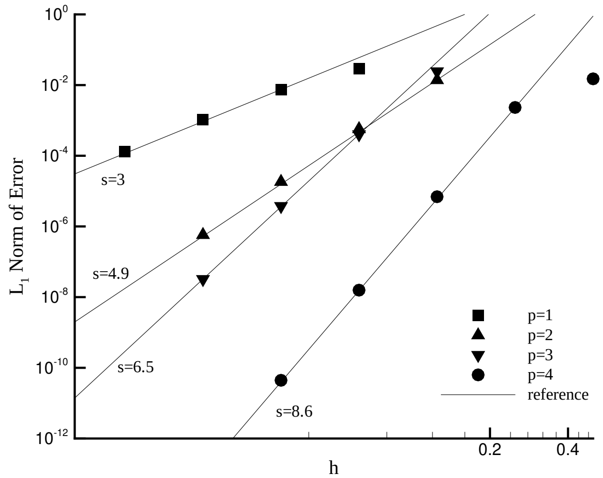

Figure 17 Mesh refinement results using a mix of triangular and quadrilateral elements shown in Figure 14. p is the order of the basis functions and s denotes the slope of the fitted convergence line.

simulations using a uniform distribution of triangular elements. Calculations for $p = 1, 2, 3$ and 4 have been carried out. The L_1 norm of the difference between the solutions at $t = t_4$ and $t = t_{20}$ has been plotted as function of the element size h. Also plotted are fitted convergence lines with their slopes indicated by s. A global convergence of order $2p + 1$ is clearly observed for $p = 1, 2$ and 3. For the case of $p = 4$, verification of the order of convergence has been found to be more difficult as the L_1 norm itself is fast approaching machine zero.

The mesh refinement results for a grid with a mix of triangles and squares are shown in Figure 17. Again, the L_1 norm of the error reduces nearly at order $2p + 1$ for $p = 1, 2, 3$ and 4.

Conclusions

An analysis of two-dimensional waves in a discontinuous Galerkin scheme has been presented. The eigenvalue problem for spatially propagating waves in a uniform mesh with triangular or quadrilateral elements has been formulated. It is found that the discontinuous Galerkin scheme can support physical as well as spurious non-physical wave modes. For the physical modes, the numerical dispersion relation is accurate locally to order $2p + 2$, giving a global propagation error of order $2p+1$. The non-physical modes are highly damped and, thus, inefficient in propagating in space. Furthermore, numerical wave reflection and transmission at an interface of grid discontinuity have been studied based on the eigenvalues and eigenfunctions of the uniform grids on either side of the interface. It is found that numerical reflection due to grid discontinuity is likely to be confined near the interface. The order of convergence of propagation error has been verified by direct numerical simulations.

ACKNOWLEDGEMENT F. Q. Hu was supported by NASA Grant NAG-1-01044.

REFERENCES

1. B. Cockburn, G. E. Karniadakis and C.-W. Shu, The development of discontinuous Galerkin methods, *Discontinuous Galerkin Methods* (Cockburn et al eds), Springer, 3-50, 2000.

2. H. Atkins and C.-W. Shu, Quadrature-free implementation of discontinuous Galerkin methods for hyperbolic equations, AIAA Journal, Vol.36, 775-782, 1998.

3. T. Warburton and G. E. Karniadakis, A discontinuous Galerkin method for the viscous MHD equations, Journal of computational Physics, Vol. 152, 608-641, 1999.

4. F. Q. Hu and H. L. Atkins, Eigensolution analysis of the discontinuous Galerkin method with non-uniform grids, part I: One space dimension, ICASE Report 2001-40, also submitted to Journal of Computational Physics.

5. D. R. Durran, Wave Propagation in Quadratic-Finite-Element Approximations to Hyperbolic Equations, Journal of Computational Physics, Vol. 159, No. 2, 448-455, 2000.

6. J. F. Semblat and J. J. Brioist, Efficiency of higher order finite elements for the analysis of seismic wave propagation, Journal of Sound and Vibration, Vol. 231, Vol. 2, 460-467, 2000.

7. F. Q. Hu, M. Y. Hussainni and P. Rasetarinera, An analysis of the discontinuous Galerkin method for wave propagation problems, Journal of Computational Physics, Vol. 151, 921-946, 1999.

8. P. Rasetarinera, M. Y. Hussaini and F. Q. Hu, Some remarks on the accuracy of a discontinuous Galerkin method, *Discontinuous Galerkin Methods* (Cockburn et al eds), Springer, 407-412, 2000.

9. S. Sherwin, Dispersion analysis of the continuous and discontinuous Galerkin formulations, *Discontinuous Galerkin Methods* (Cockburn et al eds), Springer, 425-431, 2000.

Appendix

The mass and "stiffness" matrices for equation (13) are defined as follows:

$$\mathbf{Q} = \{q_{\ell\ell'}\}_{L\times L},\ q_{\ell'\ell} = \int_\Omega \phi_\ell \phi_{\ell'} d\mathbf{x}$$

$$\mathbf{Q}_x = \{q_{\ell\ell'}\}_{L\times L},\ q_{\ell'\ell} = \int_\Omega \frac{d\phi_\ell}{dx} \phi_{\ell'} d\mathbf{x}$$

$$\mathbf{Q}_y = \{q_{\ell\ell'}\}_{L\times L},\ q_{\ell'\ell} = \int_\Omega \frac{d\phi_\ell}{dy} \phi_{\ell'} d\mathbf{x}$$

$$\mathbf{B}^{(i)} = \{b_{\ell\ell'}\}_{L\times L},\ b_{\ell'\ell} = \int_{\Gamma^{(i)}} \phi_\ell \phi_{\ell'} ds$$

$$\mathbf{B}'^{(i)} = \{b'_{\ell\ell'}\}_{L\times L},\ b'_{\ell\ell'} = \int_{\Gamma^{(i)}} \phi_\ell \phi^-_{\ell'} ds$$